Direct-Drive Target Designs for the National Ignition Facility

The National Ignition Facility (NIF) is currently under construction at Lawrence Livermore National Laboratory (LLNL). One of the primary missions of the NIF is to achieve fusion ignition by means of inertial confinement fusion (ICF). Two main approaches have been considered for achieving thermonuclear yield in ICF. The first approach, known as indirect-drive ICF,[1] encloses a DT-fuel target inside a hohlraum. The laser beams are incident on the hohlraum's wall where the laser light is converted to x rays. These x rays then implode the target, leading to the ion temperature and ρR product necessary to achieve ignition. The second approach, known as direct-drive ICF, dispenses with the hohlraum and directly illuminates the laser light onto the target.

Direct drive offers a number of advantages[2] over indirect drive: (1) direct-drive designs have potentially higher gains than indirect drive; (2) direct-drive plasma coronas are not as susceptible to laser–plasma instabilities (LPI's) as indirect drive; (3) direct-drive targets are inherently less complex than indirect-drive hohlraum targets. Direct drive also has some potential disadvantages, especially the severe requirements on laser-beam uniformity.

Most of the U.S. research effort has centered on the indirect-drive approach, which is reflected in the decision to commence operations on the NIF in the indirect-drive configuration. NIF, however, is not to preclude direct drive, and it is currently expected that the NIF will be reconfigured for direct-drive operations commencing in 2009. Before the conversion to direct-drive operations, a number of modifications must be made to the NIF. First, to provide a uniform illumination of the direct-drive target, half the final optics assemblies (FOA's) must be relocated from the poles to the waist of the target chamber; second, direct-drive uniformity enhancements (2-D SSD[3] and polarization smoothing) must be added to all beamlines; and third, the cryogenic-handling system must be capable of "cradle-to-grave" operations.

This article describes the direct-drive ignition target designs developed at the University of Rochester's Laboratory for Laser Energetics (LLE). The following three sections will (1) outline the current direct-drive designs under investigation at LLE and NRL; (2) present a sensitivity study of the "all-DT" design; and (3) review the current laser and target specifications required to achieve a successful direct-drive ignition campaign on the NIF.

Direct-Drive Target Design Overview

Many common areas of physics exist between direct- and indirect-drive capsule designs. Both target designs require high compression of the DT fuel with a central high-temperature (>5-keV) ignition region. A typical implosion involves the deposition of energy (laser light in direct drive, x rays in indirect drive) on the target surface, which rapidly heats up and expands. As this *ablator* expands outward, the remainder of the shell is driven inward by the rocket effect compressing the fuel to the necessary density. The implosion can be tailored to give a number of assembled fuel configurations, such as isobaric with a uniform temperature and density in the fuel or isochoric with a high-temperature hot spot surrounding a low-temperature main fuel layer. The most energy efficient[1] configuration is isobaric with a central high-temperature *hot spot* surrounding a low-temperature *main fuel layer*. The central hot spot initiates the fusion reaction, which leads to a burn wave propagating into the main fuel layer; thus, for robust high-gain designs, it is vitally important to assemble the high-temperature hot spot and cold, dense main fuel layer accurately. For direct-drive target designs two main effects can prevent the correct assembly of the fuel: (1) preheat of the fuel and (2) hydrodynamic instabilities of the imploding shell.

Preheat of the DT fuel will increase the pressure of the fuel and thus make the target harder to compress. Preheat can arise from fast electrons, radiation, and the passage of shocks. The amount of preheat can be quantified in terms of the *adiabat α* of the implosion. The adiabat is defined as the ratio of the fuel's specific energy to the Fermi-degenerate specific energy. It can be shown that the gain G of the target scales as $\alpha^{-3/5}$. Fast electrons generated by laser–plasma processes (such as SBS, SRS, and two-plasmon decay) in the plasma corona can couple

into the fuel. These plasma processes occur when the intensity of the laser exceeds certain thresholds; thus, the control of fast-electron production constrains the maximum intensity of the design pulse. Radiative preheat and the passage of shocks are controlled by the target material and the shape of the laser pulse, respectively.

Hydrodynamic instabilities, such as the Rayleigh–Taylor instability (RTI), can seriously degrade the implosion by breaking the spherical symmetry of the implosion. The RTI occurs twice during the implosion: at the outer ablation surface as the shell accelerates inward and at the hot spot–main fuel layer interface as the capsule decelerates at the end of the implosion. Considerable theoretical,[4] numerical,[5] and experimental[6] work has demonstrated that the RT growth rate at the ablation surface is reduced from the classical value by ablative stabilization. From design simulations the ablation velocity v_a has been shown to scale as $\alpha^{-3/5}$. Another important parameter for stability considerations is the in-flight aspect ratio (IFAR). This is the ratio of the shell radius R to its thickness ΔR as the shell implodes. Higher IFAR implosions are more susceptible to hydrodynamic instabilities. Simulations have shown that the IFAR depends primarily on the square of the implosion velocity v_{imp}^2 and the adiabat ($\alpha^{-3/5}$).

Control of the isentrope of the implosion is thus important for overall target gain ($G \sim \alpha^{-3/5}$) and target stability. Indirect-drive designs are believed to be sufficiently stable to hydrodynamic instabilities that they can operate very near the Fermi-degenerate limit ($\alpha = 1$). Direct-drive designs require the implosion to operate at a higher isentrope. LLE and NRL are currently investigating three designs (see Fig. 79.1) that use various combinations of shock and radiative heating to control the isentrope.

The first design [Fig. 79.1(a)] employs a solid (cryogenic) DT-shell target with a thin polymer ablator (required to fabricate the cryogenic shell) surrounding the DT-ice shell.[7] For this design the DT acts as both the fuel and the ablator. This design uses shock preheat to control the isentrope of the ablation surface and the fuel.

The second design [Fig. 79.1(b)] employs a low-density foam surrounding a clean cryogenic DT layer (a thin barrier layer separates the foam layer from the DT). The foam layer acts as the ablator. This design uses shock preheat to control the isentrope, but it offers the flexibility of placing the ablation surface and main fuel layer on different isentropes.

The third design [Fig. 79.1(c)] places a high-Z coating over a DT wicked foam ablator, which encases a pure-DT ice layer.[2] This design uses mainly radiative preheat. By carefully selecting the radiative properties of the high-Z ablator, it is possible to preferentially heat the carbon in the foam, boosting the isentrope of the ablation surface, while leaving the fuel on a lower isentrope.

Although the "all-DT" design has the disadvantage that the fuel and ablator are on the same adiabat, it has a number of significant advantages. First, the target is very simple, with no classically unstable RTI interfaces. Second, DT has a very high ablation velocity, which reduces the RTI at the ablation surface. Third, a DT ablator potentially gives higher hydrodynamic efficiencies, thus maximizing the achievable gain. Because of these considerations, a scaled version of this target design has been selected for experimental investigation on the OMEGA laser and is used as the base-line design for establishing the detailed specifications for the NIF. The next section presents a more-detailed review of the all-DT design.
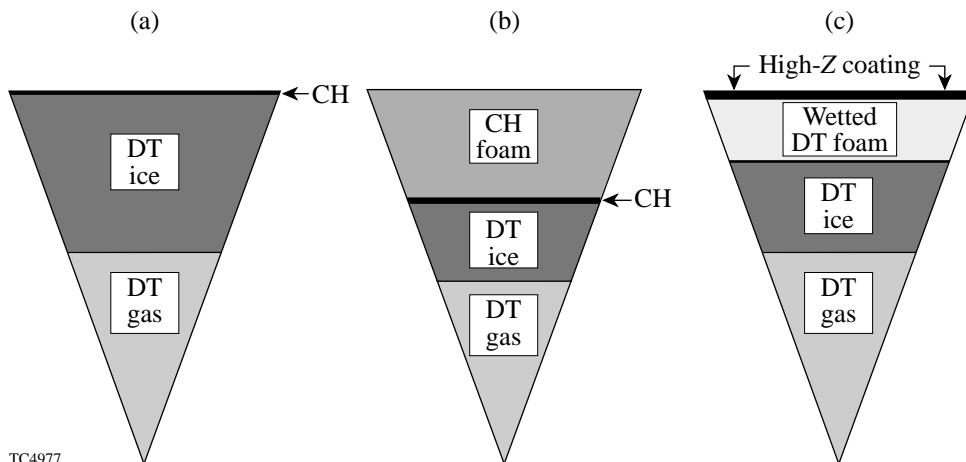

Figure 79.1
Schematic of the direct-drive target designs. (a) The all-DT target design, which relies on shock heating to select the adiabat. (b) The foam ablator design, which relies on shock heating to select the adiabat separately for the ablator and the fuel. (c) The radiative design, which relies on radiative absorption to select the adiabat for the ablator.

TC4977

The Baseline All-DT Target Design

Figure 79.2 shows the gain curves constructed by LLE during the design phase of the NIF[7] for laser energies from 1 to 2 MJ and for implosions on isentropes from $\alpha = 1$ to 4. Variation in the isentrope was achieved by varying the incident laser pulse shape. Based on the results of current OMEGA experiments and theoretical calculations of these NIF designs, we have selected the 1.5-MJ, $\alpha = 3$ continuous-pulse design to be the baseline design for further study. Figure 79.3(a) shows the target specification; Fig. 79.3(b) shows the pulse shape for this design. This pulse shape consists of two distinct temporal

regions: the foot and the main drive. The DT-ice thickness and adiabat of the implosion determine the length and duration of the foot. In this design, the foot is 4.25 ns long at a power of 10 TW. This region launches a 10-Mbar shock through the DT ice. At the time of shock breakout at the rear surface of the DT ice, the pulse ramps up to the drive region, which lasts for 2.5 ns at a power of 450 TW. This rapid rise in intensity generates pressures of approximately 80 Mbar and thus accelerates the DT ice inward. Different adiabats can be achieved by varying the length and intensity of the foot and carefully shaping the rise to the drive pulse. For example, an $\alpha = 2$ design has a longer, lower-intensity foot and a gentler-rising transition region.

The $\alpha = 3$ design is predicted, by 1-D calculations, to have a gain of 45, a neutron-averaged ion temperature of 30 keV, and a neutron-averaged $\rho R = 900$ mg/cm^2. The peak IFAR of this design is 60, and the hot-spot convergence ratio is 29. The conditions near peak compression ($t = 10.4$ ns) are shown in Fig. 79.4.

These direct-drive designs have two distinct shocks: the first is launched at the start of the pulse; the second is generated during the rise to the main drive intensity. Figure 79.5 is a contour map of the radial logarithmic derivative of the pressure [d(lnP)/dr] as a function of Lagrangian coordinate and time. The darker, more-intense regions represent a larger gradient in pressure and thus capture the position of the shocks. The timing between these two shocks determines the gain of the target design. When the first shock breaks out of the DT-ice layer (at 5.8 ns), a rarefaction wave expands outward from the rear surface of the DT ice. If the second shock arrives too late, the shock travels through a decreasing density gradient, which
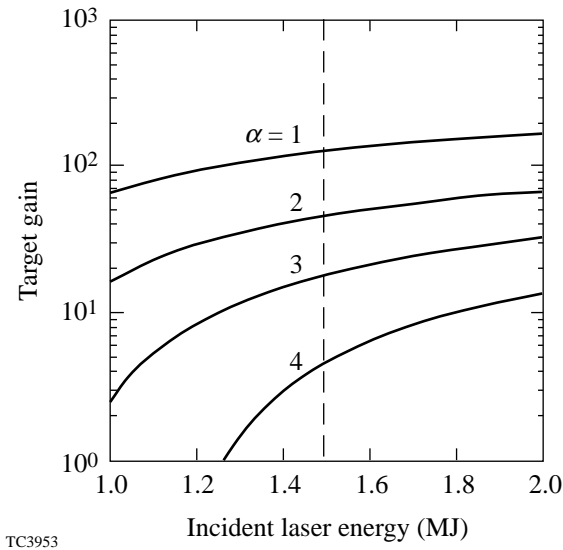

TC3953

Figure 79.2
The gain curves constructed at LLE for various isentropes and incident laser energies. The dashed line corresponds to the NIF baseline 1.5-MJ energy.
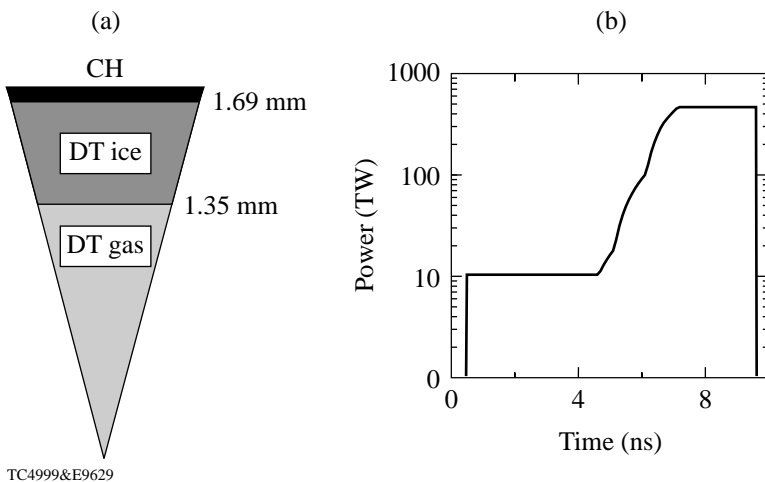
(a)

CH

1.69 mm

DT ice

1.35 mm

DT gas

TC4999&E9629

(b)

Time (ns)

Figure 79.3
The baseline, $\alpha = 3$, "all-DT," 1.5-MJ target design. (a) The target specification and (b) the pulse shape.

TC4946
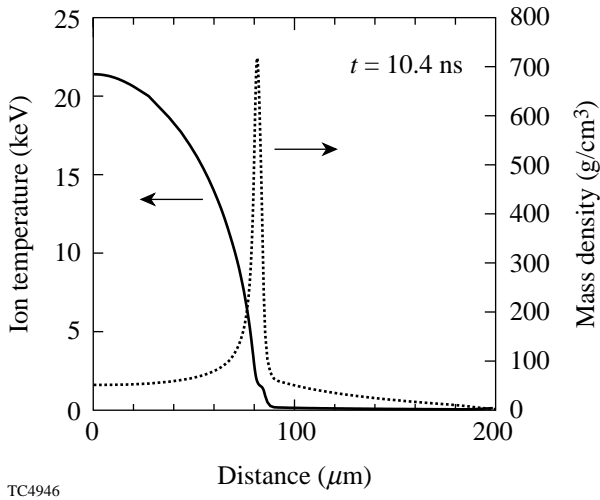
Figure 79.4
The ion temperature (solid line) and the mass density (dotted line) near peak compression for the $\alpha = 3$ baseline design.
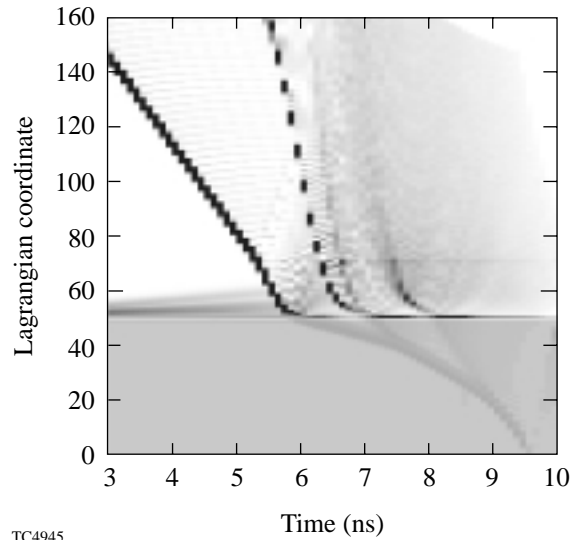

TC4945

Figure 79.5
Shock propagation as shown by a contour map of the logarithmic derivative of the pressure as a function of time and Lagrangian coordinate. The interface between the DT ice and gas is at Lagrangian marker 50.

increases the shock strength. This puts the main fuel layer onto a higher adiabat and thus reduces the gain. Conversely if the second shock arrives too early, the hot spot produces the burn wave before the main fuel layer has reached peak density and thus reduces the overall target gain. An error in shock timing can arise from the following:

1. Inadequate Control of the Laser Pulse Shape

The $\alpha = 3$ laser pulse shape is essentially defined by eight temporal points as shown in Fig. 79.6. To establish the sensitivity of the target design to variations in pulse shape we performed a series of 1-D calculations. These calculations involved varying the power and temporal position of each point (while holding the other points fixed). By adjusting the last point of the laser pulse we ensured that the overall energy in the pulse remained constant at 1.5 MJ. If a temporal point was adjusted to be in front of another point, that point was removed from the pulse. Figure 79.6 shows the contours of gain generated by moving five of the points. Note that as the first point moves earlier in time (thus lengthening the foot region), the power must drop to preserve target gain; however, reduced foot intensity leads to a weaker shock formation, thus reducing the adiabat of the target and leading to a more unstable implosion. We can see that target performance is sensitive to the foot and transition regions of the laser pulse, but is relatively insensitive to the details of the high-power region. Figure 79.7(a) shows the target gain as a function of a change in the foot power. Figure 79.7(b) shows the target gain as a
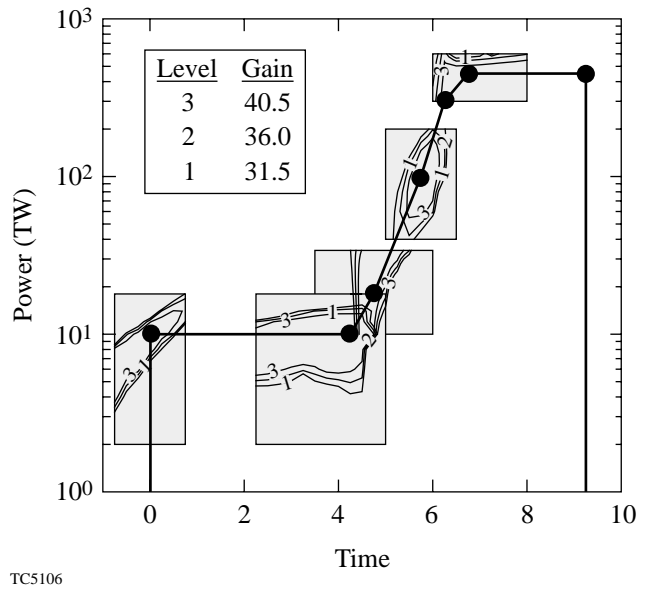

TC5106

Figure 79.6
The $\alpha = 3$ pulse shape with overlaid contours of gain. The circles correspond to the temporal points used to define the pulse shape. The contours correspond to the gain that would be achieved if the temporal point was moved to that time and power location (holding all other points fixed).

function of the length of the foot region. From these curves it has been established that the pulse power in the foot region must be controlled and measured to ±3%, and that the pulse duration is controlled and measured to ±50 ps. These curves suggest a possible "tuning" strategy for the NIF. By varying the length of the foot (and holding the other portion of the pulse constant) we can scan through the optimal gain region and adjust for uncertainties in the shock transit through the DT ice.

2. Uncertainties in the Target's Equation of State (EOS)

1-D simulations with *SESAME* tables, analytic Thomas-Fermi, and Livermore DT-ice tables have been performed to address the uncertainties in EOS. Using the tuning strategy of foot-length and intensity variations, we can optimize the gain for different EOS models. For example, the optimal gain for targets modeled using the analytic Thomas-Fermi EOS required a 600-ps reduction in foot length from the *SESAME*

case. Although we have established that the designs can be retuned to these EOS models, experimental measurements of the EOS of D_2 ice, D_2 wicked foam, and high-Z-doped plastics are required to accurately model the target.

3. Uncertainties in Target Thickness

A series of 1-D simulations have been performed to establish the required control of the DT-ice thickness (which is controlled by the DT-gas-fill pressure). Specifying the control of the ice thickness determines the control and measurement of the fill pressure during ice layering. Figure 79.8 shows the gain as a function of ice-layer thickness (holding the outer radius of the shell fixed). A variation of ±5 μm in a total ice thickness of 340 μm leads to a 2% reduction in gain. This corresponds to a control of the DT-fill pressure of ~20 atm out of a total fill pressure of 1020 atm (at room temperature).
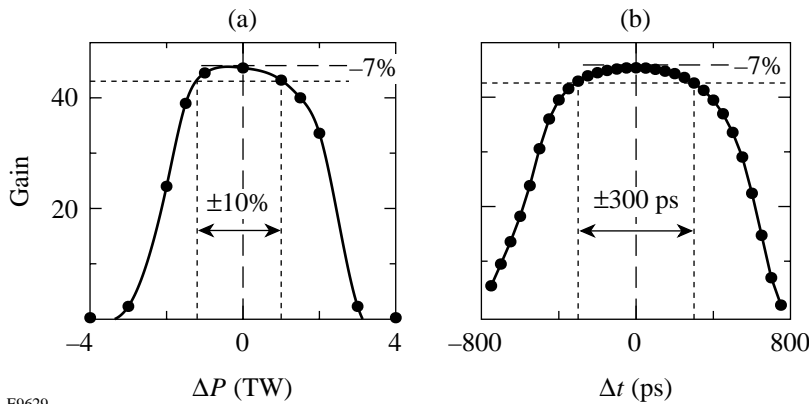

Figure 79.7
The target gain as a function of the change in (a) the foot power and (b) the foot duration from the nominal 10-TW, 4.25-ns parameters.
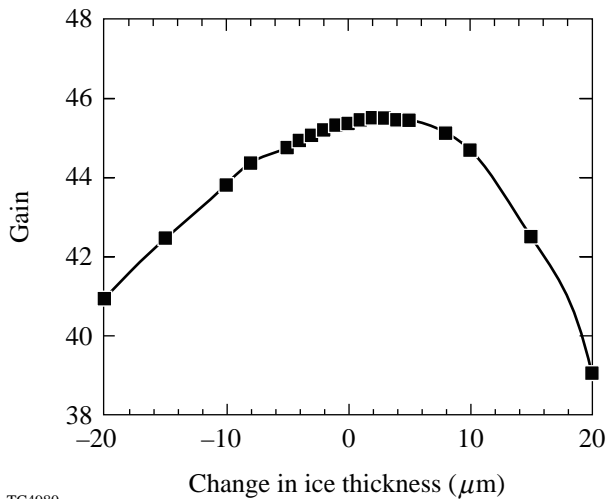

Figure 79.8
The target gain as a function of the change in the ice-layer thickness.

The need to control the hot-electron fraction is similar to the indirect-drive requirements, namely that less than 0.1% of the laser energy is deposited in the DT fuel via hot electrons. Since the laser is more closely coupled to the target in direct drive, however, the transport of hot electrons to the target is more efficient, and the targets are therefore more sensitive to hot electrons than in indirect drive. 1-D simulations were performed with various percentages of laser energy dumped at the critical surface into an 80-keV hot-electron tail. These hot electrons were transported through the target where approximately 4% of the energy absorbed into fast electrons was deposited in the DT-ice fuel layer. Figure 79.9 shows the effect of between 1% and 3% laser energy absorbed into fast electrons on the gain. A 30% reduction in gain occurred when 1% of the incident laser energy was absorbed into fast electrons. The hot electrons are produced by laser–plasma instabilities (LPI's), such as SRS, SBS, and two-plasmon decay.
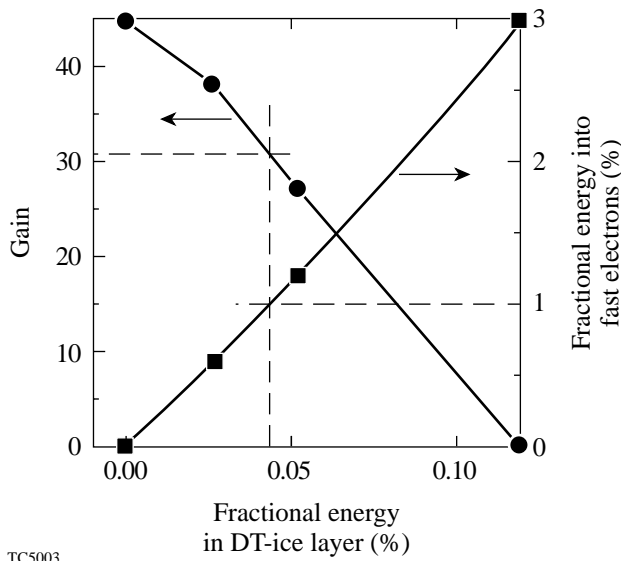

TC5003

Figure 79.9
The effect of varying the fraction of energy dumped into an 80-keV hot-electron tail on the target gain.

Figure 79.10(a) shows the threshold intensities for SRS and SBS; Fig. 79.10(b) shows the total NIF intensity at the quarter- and tenth-critical surfaces. At each time the minimum threshold in the corona is calculated based on simulations of the $\alpha = 3$ density and velocity profiles. For SRS the threshold is seen to be well above the total NIF intensity at tenth-critical; this is the most relevant density since the minimum thresholds tend to occur far out in the corona where scale lengths are long and densities are low. The single-cluster NIF intensity would be lower by a factor of about 12. For SBS the total intensity is

well above threshold after about 6 ns, while the single-cluster intensity is comparable to the threshold. Further study is required to determine how many clusters are likely to participate in driving SBS. SBS has a low threshold at this time because the NIF pulse is rapidly increasing in intensity, producing a local velocity minimum in the density profile and a correspondingly long velocity scale length. These thresholds are calculated on the basis of inhomogeneity scale lengths; the density scale length is the determining factor for SRS and the velocity scale length for SBS. Damping has little effect on the minimum thresholds; the damping contribution depends on the product of the electromagnetic wave damping (mostly collisional, small at low densities) and the electrostatic wave damping (mostly Landau). The Landau damping becomes large for electron-plasma waves (SRS) at low densities and for ion-acoustic waves (SBS) when T_i approaches T_e. The minimum threshold for both instabilities tends to occur at low densities where the small damping of the electromagnetic wave makes the contribution to the threshold negligible. Large Landau damping of the electrostatic waves may, however, substantially reduce growth rates even if the instability is above threshold.

A high level of illumination uniformity is required to achieve ignition. Both direct- and indirect-drive designs require that the targets be driven by pressure nonuniformity levels of less than 1% rms. The angular variation in the intensity distribution on the target is routinely described in terms of spherical-harmonic modes. An ℓ-mode is related to the target radius R and the nonuniformity wavelength λ through $\ell = 2\pi R/\lambda$. The mode spectrum is normally divided into two regions: a low ℓ-mode region ($\ell < 20$) and a high ℓ-mode region ($20 < \ell < 500$). Indirect drive benefits from the conversion of the laser light to x rays. Essentially all modes above $\ell = 10$ are eliminated by x-ray conversion. In direct drive the laser beam alone must achieve the desired level of uniformity; thus, direct drive places much tighter tolerances on the single-beam uniformity and beam-to-beam balance than indirect drive.

Low ℓ-mode (long-wavelength) perturbations are seeded by beam-to-beam variations arising from (1) the mispointing or misfocusing of the laser beams, (2) a lack of energy and power balance, or (3) mispositioning of the target. Such modes grow secularly during the implosion. A simple argument is used to calculate the maximum tolerable variation in the low ℓ-mode spectrum. Since these modes grow secularly, the final distortion δr_f of the compressed fuel at average radius r_f is given by $\delta r_f = \Delta a t^2$, where Δa is the acceleration nonuniformity and t is the implosion time. For a shell initially at radius r_0 the

distortion of the shell is given by $\delta r_f / r_f = \Delta a / a \left(r_0 / r_f - 1 \right)$. Numerical calculations using the 2-D hydrocode *ORCHID* suggest that final core distortions of 50% can be tolerated; thus, for a convergence ratio of 25 (which is typical for direct-drive targets), a peak-to-valley acceleration nonuniformity of 2% can be tolerated. The laser nonuniformity in the low ℓ-mode region must be maintained below 1% rms.

The high ℓ-mode (short-wavelength) region is seeded by the structure within the individual laser beam. These modes excite the Rayleigh–Taylor instability, which causes the modes to grow much more rapidly than in the low ℓ-mode region. Note that extremely high mode numbers are not important since they are ablatively stabilized, rapidly saturate, and do not feed through to the hot-spot region.

The effect of the growth of the hydrodynamic instabilities has been examined by two techniques: The first technique uses detailed 2-D *ORCHID* simulations to directly determine the effects of perturbation on target performance. This technique is computationally intensive and does not give the correct 3-D multimode saturation of the RT instability. The second technique uses a postprocessor to the 1-D simulations. This postprocessor uses a self-consistent model[8] to study the evolution of perturbations at the ablation front and the back surface of an accelerated spherical shell. The model includes the ablative Richtmyer–Meshkov (RM),[9] RT, and Bell–Plesset (BP) instabilities; 3-D Haan saturation[10] is included. The model consists of two differential equations (describing the ablation- and inner-surface perturbations) obtained by solving the linearized conservation equations in the DT gas, the shell, and the blowoff plasma regions. The overdense–ablated plasma interface is approximated as a surface of discontinuity.[11]

Direct-drive target designs must tolerate four sources of nonuniformity to ignite and burn: (1) inner-DT-ice roughness, (2) outside CH capsule finish, (3) drive asymmetry, and (4) laser imprinting. Multidimensional simulations of the deceleration phase have shown that our design will ignite when the inner-surface nonuniformity is less than 1.5 μm at the start of the deceleration phase. By performing an extensive series of calculations with various levels of nonuniformity, it is possible to establish the requirements for the four seed terms.

The hardest seed term to establish is that for laser imprint. A series of planar 2-D simulations have been performed using *ORCHID*. These simulations determined the imprint efficiency for single modes of irradiation nonuniformity. The effect of 2-D SSD was included using the approximation

$$\sigma_{\text{rms}} \sim \sqrt{t_c/t} \,,$$

where

$$t_c = \left[\Delta \nu \sin \left(k\Delta/2 \right) \right]^{-1}$$

is the coherence time, $\Delta \nu$ is the bandwidth, k is the wave number of the spatial-intensity nonuniformity, and Δ is the speckle size. For example, using a phase-plate nonuniformity spectrum with 1 THz of bandwidth, the laser will imprint a surface nonuniformity equal to $\sigma_{\text{rms}} = 360$ Å (in modes $\ell < 1000$) at the start of the acceleration phase. The additional sources of nonuniformity are then added to that from the laser. For example, Fig. 79.11 shows the mode spectrum of the ablation surface at the start of the acceleration phase for the case of a 1-THz-bandwidth, perfectly uniform outer shell and
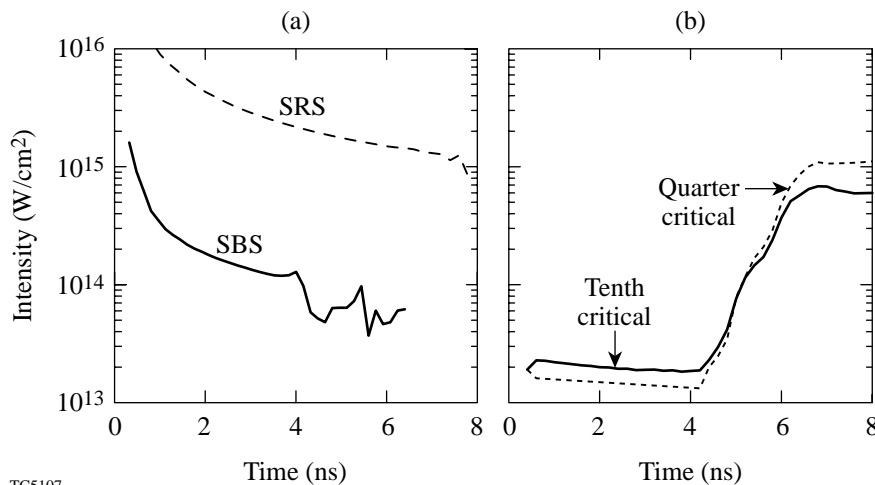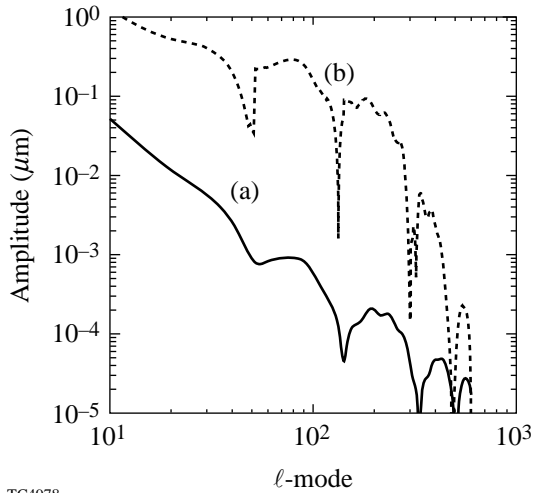

Figure 79.10
(a) The SBS (solid line) and SRS (dashed line) thresholds calculated from the density and velocity profiles as a function of time for the baseline target design. (b) The combined, overlapped beam intensity at the quarter- (dashed line) and tenth-critical (solid line) surfaces as a function of time.

TC5107

an additional $\sigma_{rms} = 1300$-Å perturbation, which has accumulated from the feed-out of 0.5-μm rms from the inner DT-ice layer. Figure 79.11 also shows the mode spectrum of the ablation surface at peak shell velocity, which defines the end of the acceleration phase. The sum of the amplitude of the individual modes gives the total mix width of the ablation-surface instability. Figure 79.12 shows the mix width and the shell thickness as a function of time. In this example we can

clearly see that the shell is larger than this mix width, so we conclude that the $\alpha = 3$ design will survive the acceleration phase when we have 1 THz of bandwidth and 0.5-μm rms of inner DT-ice roughness. At the end of the deceleration phase the total nonuniformity on the inner surface is 1.3 μm, so we would expect this design to ignite.

Figure 79.13 shows the combined effect of different laser-uniformity levels and inner-ice-surface roughness for two different outer-surface finishes on the perturbation amplitude

TC4978

Figure 79.11
The mode spectrum of the outer ablation surface at (a) the start of the acceleration phase and (b) the start of the deceleration phase.
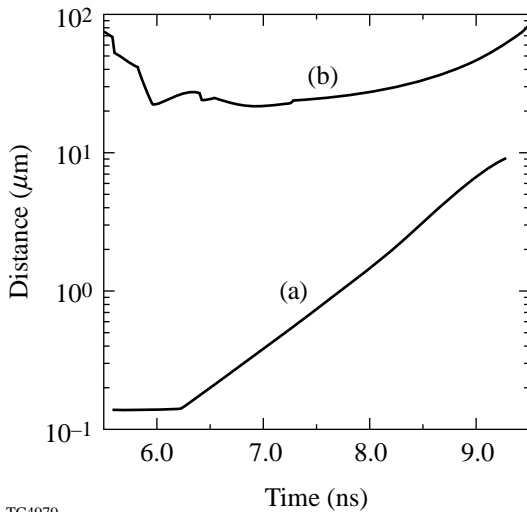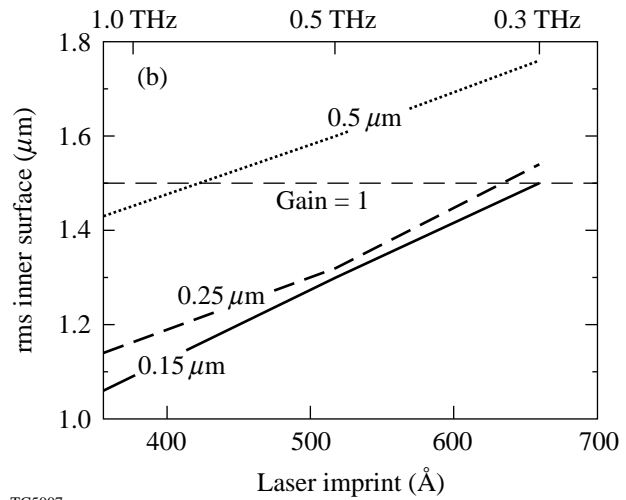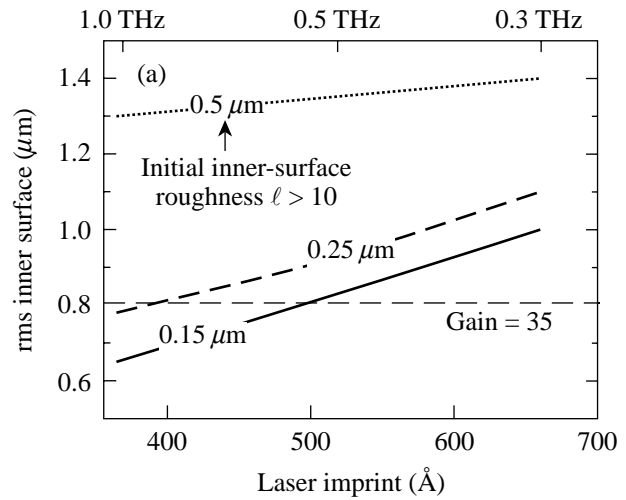

TC4979

Figure 79.12
The (a) ablation-surface amplitude and (b) the shell thickness as a function of time up to the end of the acceleration phase for the baseline, $\alpha = 3$, all-DT target design with 1-THz, 2-D SSD and 0.5-μm initial inner surface, DT-ice finish.

TC5007

Figure 79.13
The combined effect of laser uniformity and inner DT-ice surface roughness (for modes greater than 10) on the rms inner-surface amplitude at the end of the acceleration phase for (a) 0-Å outer-surface finish and (b) 840-Å outer-surface roughness.

of the inner surface at the time of deceleration. For example, 0.5 THz of bandwidth is equivalent (from *ORCHID* simulations) to 520 Å of initial outer-surface perturbation. This is combined with 0.5 μm of inner-surface roughness and with a perfect outer-surface finish [Fig. 13(a)]. The resultant amplitude at deceleration is 1.35 μm. When there is 840 Å [Fig. 13(b)] of outer-surface roughness, the amplitude of the inner surface at deceleration rises to 1.45 μm. These final amplitudes are very close to the maximum tolerable, so we conclude for safety that for a successful ignition campaign using direct drive we will need 1 THz of bandwidth, < 0.25 μm of DT-ice nonuniformity in mode $\ell > 10$, and < 800 Å of outer-surface perturbation.

Conclusions

Based on the calculations described in the previous section we have established specifications required on the NIF to ensure a successful direct-drive ignition campaign. Table 79.I summarizes these requirements. It should be noted that independent calculations by Weber,[12] using the 2-D *LASNEX* code, confirm our calculations that the $\alpha = 3$ continuous-pulse design will survive the acceleration phase and should achieve ignition.

Table 79.I: Summary of the specifications for our current modeling of the baseline "all-DT" target design.

Parameter	Requirements
Laser energy	1.5 MJ
Pulse shape	50:1 contrast, 10-ns duration [see Fig. 79.3(b)]
Beam-to-beam power balance	8% in 500 ps
Quad-to-quad power balance (assuming independent quads)	4% in 500 ps
Laser bandwidth	1 THz
Individual beam nonuniformity	3% in 500 ps (all modes)
Outer CH	<2 μm
Outer-surface target finish	<800 Å
Inner DT-ice thickness	340 μm$\pm$5 μm
Inner DT-ice-layer uniformity	<0.25 μm ($\ell > 10$) (for $\ell < 10$ exact value to be determined)
Shock-timing accuracy	<50 ps
Preheat	$<0.1\%$ of incident laser energy

REFERENCES

1. J. D. Lindl, Phys. Plasmas **2**, 3933 (1995).

2. S. E. Bodner, D. G. Colombant, J. H. Gardner, R. H. Lehmberg, S. P. Obenschain, L. Phillips, A. J. Schmitt, J. D. Sethian, R. L. McCrory, W. Seka, C. P. Verdon, J. P. Knauer, B. B. Afeyan, and H. T. Powell, Phys. Plasmas **5**, 1901 (1998).

3. S. Skupsky, R. W. Short, T. Kessler, R. S. Craxton, S. Letzring, and J. M. Soures, J. Appl. Phys. **66**, 3456 (1989).

4. H. Takabe *et al.*, Phys. Fluids **28**, 3676 (1985); R. Betti, V. N. Goncharov, R. L. McCrory, and C. P. Verdon, Phys. Plasmas **2**, 3844 (1995).

5. M. Tabak, D. H. Munro, and J. D. Lindl, Phys. Fluids B **2**, 1007 (1990); C. P. Verdon, R. L. McCrory, R. L. Morse, G. R. Baker, D. I. Meiron, and S. A. Orszag, Phys. Fluids **25**, 1653 (1982); J. H. Gardner, S. E. Bodner, and J. P. Dahlburg, Phys. Fluids B **3**, 1070 (1991).

6. J. P. Knauer, C. P. Verdon, D. D. Meyerhofer, T. R. Boehly, D. K. Bradley, V. A. Smalyuk, D. Ofer, P. W. McKenty, S. G. Glendinning, D. H. Kalantar, R. G. Watt, P. L. Gobby, O. Willi, and R. J. Taylor, in *Laser Interaction and Related Plasma Phenomena*, edited by G. H. Miley and E. M. Campbell (American Institute of Physics, New York, 1997), Vol. 406, pp. 284–293; J. Knauer, R. Betti, D. K. Bradley, T. R. Boehly, T. J. B. Collins, V. N. Goncharov, P. W. McKenty, D. D. Meyerhofer, V. A. Smalyuk, C. P. Verdon, S. G. Glendinning, D. H. Kalantar, and R. G. Watt, "Single-Mode Rayleigh-Taylor Growth-Rate Measurements with the OMEGA Laser System," to be published in Physics of Plasmas; J. Grun *et al.*, Phys. Rev. Lett. **58**, 2672 (1987); S. G. Glendinning, S. N. Dixit, B. A. Hammel, D. H. Kalantar, M. H. Key, J. D. Kilkenny, J. P. Knauer, D. M. Pennington, B. A. Remington, R. J. Wallace, and S. V. Weber, Phys. Rev. Lett. **78**, 3318 (1997).

7. C. P. Verdon, Bull. Am. Phys. Soc. **38**, 2010 (1993).

8. V. N. Goncharov, "Self-Consistent Stability Analysis of Ablation Fronts in Inertial Confinement Fusion," Ph.D. thesis, University of Rochester, 1998.

9. V. N. Goncharov, Phys. Rev. Lett. **82**, 2091 (1999).

10. S. W. Haan, Phys. Rev. A **39**, 5812 (1989).

11. A. R. Piriz, J. Sanz, and L. F. Ibanez, Phys. Plasmas **4**, 1117 (1997).

12. S. V. Weber *et al.*, *ICF Quarterly Report* **7**, 43, Lawrence Livermore National Laboratory, Livermore, CA, UCRL-LR-105821-97-2 (1997).